

Supplementary Information

Interplay between short-range attraction and long-range repulsion controls reentrant liquid condensation of ribonucleoprotein-RNA complexes

Ibraheem Alshareedah, Taranpreet Kaur, Jason Ngo, Hannah Seppala, Liz-Audrey Djomnang Kounatse, Wei Wang, Mahdi Muhammad Moosa, and Priya R. Banerjee*

Department of Physics, University at Buffalo, Buffalo NY 14260

*Corresponding author: Priya R. Banerjee (prbanerj@buffalo.edu); Phone: +1 (716) 645-3444.

Materials and Methods:

Peptide and RNA sample preparation: [RGRGG]₅, [KGKGG]₅, and RGG-3 domain of FUS (FUS^{RGG3};472-505) were synthesized by GenScript USA Inc. (NJ, USA; ≥ 90% purity) and were used without further purification. All peptide sequences contain a C-terminal cysteine for site specific fluorescence labeling. Concentrated stock solutions were made using RNase-free water (Santa Cruz Biotechnology) containing 50 mM dithiothreitol (DTT) to prevent cysteine oxidation. Polyuridylic acid (poly(U); molecular weight = 600-1000 kDa) and polyadenylic acid (poly(A); molecular weight = 100-500 kDa) were purchased from Sigma-Aldrich. RNA stock solutions were prepared in RNase-free water (Santa Cruz Biotechnology) and concentrations were determined by the absorbance at 260 nm using a NanoDrop oneC UV-Vis spectrophotometer. Inorganic polyphosphate (poly(P); medium chain; ~ 45-160 phosphate units) was purchased from Kerafast (Boston, MA) and stock solutions were made using RNase-free water (Santa Cruz Biotechnology).

Protein samples: The C-terminal RNA-binding domain of FUS (FUS^{R/G-rich LCD}; 211-526Δ422-453) was prepared as described before¹. FUS^{R/G-rich LCD} was expressed in E. coli cells (BL21(DE3)) and then extracted using a french press. His₆-tagged proteins were subsequently purified using Ni-NTA agarose matrix. To check the purity of the proteins, polyacrylamide gel electrophoresis (PAGE) and Coomassie blue staining were used. Concentrations of the protein samples were determined using absorbance at 280 nm (extinction coefficient: 86,750 M⁻¹.cm⁻¹ for His6-MBP-FUS^{R/G-rich LCD}; <https://web.expasy.org/protparam>). The protein samples were flash frozen in individual aliquots, stored at -80 °C and thawed prior to experiments.

Fluorescence labeling of peptides and proteins: Individual peptides and the A313C variant of FUS^{R/G-rich LCD} were site-specifically labeled using Alexa488 or Alexa594 dyes (C5-maleimide derivative, Molecular Probes) using cys-maleimide chemistry as described in our earlier works¹⁻⁵. Briefly, the labeling reactions were carried out at 4 °C overnight in the dark. Excess free dyes from FUS^{R/G-rich LCD} reaction mixture were removed by centrifugal filtration with a 3K cutoff filter (Millipore). For the peptides, excess dyes were removed by four rounds of acetone precipitation. Four times the sample volume of cold (-20°C) acetone was added to the reaction mixture. The reaction was then vortexed and incubated at -20°C for 1-2 hrs, followed by centrifugation at 12,000 × g for 10 minutes and decantation of the supernatant. After four rounds, the acetone was allowed to evaporate and the resulting dry purified labeled peptide pellet was resuspended in RNase-free water. Purity of the labeled protein was tested via SDS-PAGE. A313C variant of FUS^{R/G-rich LCD} was expressed and purified using similar protocol as the wild-type protein. UV-Vis absorption measurements were used to measure the labeling efficiencies (≥ 85% in all cases).

Solution Turbidity measurements: Peptide and RNA mixtures were prepared at 100 μM peptide concentration with variable RNA concentrations. The buffer contained 25 mM Tris-HCl (pH 7.5) and 20 mM DTT. The absorbance was measured at 350 nm using a NanoDrop oneC UV-Vis spectrophotometer at room temperature after ~100 seconds of sample equilibration with a 1.0 mm optical path length. Each turbidity plot was generated via gradual RNA titration³. Measurements were performed in triplicates. The phase boundary curve was obtained by plotting the data using OriginPro software.

Phase diagram analysis: Binary phase diagrams were constructed by measuring phase boundary curves of peptide-RNA mixtures with variable starting concentrations of a given peptide using turbidity measurements in conjunction with optical microscopy. Each sample was first subjected to turbidity measurement and subsequently placed under a Primo-vert inverted iLED microscope (Zeiss; using either 40x or 100x objective lens), equipped with a Zeiss Axiocam 503 monochrome camera. The droplets were

clearly visible for samples with a measured solution turbidity value of ~ 0.25 or higher (10 mm path length) at 350 nm. Condensation and decondensation points (x_c and x_d) were determined by this cutoff values of A350. The maximum phase separation points (x_0) were determined by the peak value of A350 at the RNA-peptide concentration plane.

Fusion of suspended droplets using optical traps: Controlled fusion assays were conducted to investigate the mesoscale dynamics of RNA-peptide droplets, as previously described¹. Briefly, each sample was injected into a tween 20-coated (20% v/v) 25 mm x 75 mm x 0.1 mm single chamber of the custom-made flow cell. Samples were prepared at concentrations that correspond to the peak in solution turbidity plot, i.e., 1.00 mg/ml peptide and 0.75 mg/ml RNA, in a buffer containing 25 mM Tris-HCl, 25 mM NaCl, and 20 mM DTT (pH 7.5). For FUS^{RGG3} fusion experiments, samples were prepared at 0.33 mg/ml peptide concentration and 0.25 mg/ml RNA concentration (RNA:peptide = 0.75) in a buffer containing 25 mM Tris-HCl, 125 mM NaCl, and 20 mM DTT (pH 7.5). FUS^{R/G-rich LCD} samples were prepared at 1.0 mg/ml protein and 0.075 mg/ml RNA in the same buffer as FUS^{RGG3}. Droplets were trapped using a dual-trap optical tweezer system coupled to a laser scanning confocal fluorescence microscope (LUMICKSTM, C-trap). Two droplets were independently trapped using optical traps operating at minimum power (to minimize heating of the trapped droplets) and then brought into close proximity. The trapping of the droplets by a 1064 nm laser was achieved due to a significant difference in the refractive index between the droplet and dispersed phases. Trap-2 was kept fixed in space and trap-1 was set to move at a constant speed of 100 nm/s in the direction of trap-2. Once the trapped droplets fuse and relax to a spherical shape, the trap motion was stopped and the force-time signal was analyzed. The force on the moving trap (i.e., trap-1) was recorded at 78.4 kHz sampling frequency (i.e., $\sim 12 \mu s$ time interval) and analyzed using an appropriate fusion relaxation model⁶. The following equation was used to fit the force-time curve:

$$F = ae^{(-t/\tau)} + bt + c \quad (1)$$

Where the parameter τ is the fusion relaxation time. The 2nd term in equation (1) is used to account for the trap's constant velocity. We recorded at least 10-15 controlled fusion events per sample, then scaled every relaxation time by the average size of the fusing droplets. A representative force relaxation curve is shown in Figure S1.

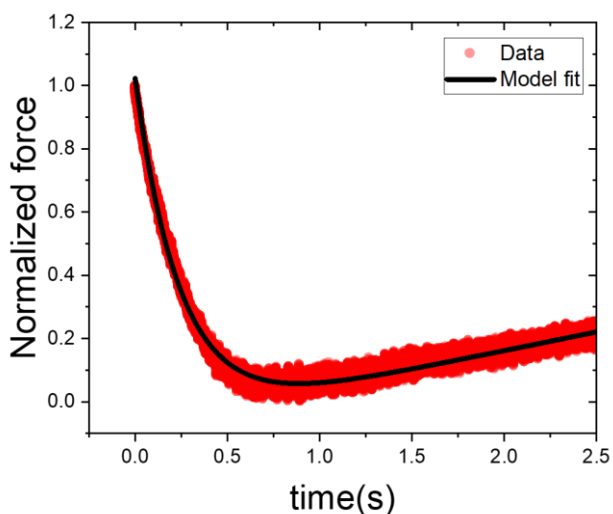


Figure S1: Representative normalized force relaxation curve during trap-induced coalescence of suspended peptide-RNA droplets. The data (red trace) is fitted (black line) using a previously published model, as described by equation-1.

FRAP measurements and confocal images of the condensates: Fluorescence recovery after photobleaching (FRAP) was measured using a Zeiss LSM710 laser scanning confocal microscope, equipped with a 63x oil-immersion objective (Plan-Apochromat 63x/1.4 oil DIC M27). Samples were incubated in a tween-coated (20% v/v) Nunc Lab-Tek Chambered Coverglass (ThermoFisher Scientific Inc.) at room temperature. For FRAP measurements, samples were prepared by mixing 1.00 mg/ml of peptide and 0.75 mg/ml of RNA (corresponding to the peak position in their turbidity plot) in 25 mM Tris-HCl, 20 mM DTT, and 25 mM NaCl (pH 7.5). Alexa488-labeled peptides (excitation/emission wavelengths were 488 nm/503-549 nm) were used as fluorescence probes in these experiments. Each FRAP curve was obtained by bleaching a specific region of interrogation (ROI) for ~ 6 s with the maximum available laser power and subsequently recording the intensity trace of the bleached ROI for approximately 300 seconds or until full recovery. FRAP curves were corrected for photo-fading using a reference ROI from an unbleached droplet. Normalized and corrected intensity time-traces were plotted using OriginPro software and corresponding images were processed using Fiji⁷. For FRAP measurements of the FUS^{R/G-rich LCD} samples, a protein concentration of 1.0 mg/ml and an RNA concentration of 0.075 mg/ml were used in 25 mM Tris-HCl, 20 mM DTT, and 125 mM NaCl (pH 7.5). Prior to the FUS^{R/G-rich LCD} droplet formation, the His₆-MBP tag was cleaved off by TEV protease, as described previously¹. The RNA concentrations were chosen according to the peak position of the turbidity plots for different RNAs. The diffusion coefficient for FUS^{R/G-rich LCD} within the condensates was calculated in a similar manner as described in our earlier work¹.

Fluorescence micrographs and FRAP data of the cluster phase were recorded using the same microscope. The cluster phase samples with poly(A) RNA were made using 2.0 mg/ml peptide and 8.0-10 mg/ml RNA (past the charge inversion point) in 10 mM Tris-HCl buffer, 20 mM DTT (pH 7.5) with variable concentrations of NaCl as described in the text and/or figure legends. The cluster phase samples with poly(U) RNA were prepared using similar peptide-RNA concentrations in 5 mM Tris-HCl buffer, 20 mM DTT (pH 7.5) with variable concentrations of NaCl as described in the text and/or figure legends.

Electrophoretic mobility and size measurements: Electrophoretic mobility of peptide-RNA complexes was measured with a dynamic light scattering (DLS) setup (ZetasizerNano ZS; Malvern Instruments Ltd.) using M3-PALS (Phase Analysis Light Scattering) technique³. Samples were prepared at 100 μ M peptide concentration (0.22 mg/ml for [KGKGG]₅ and 0.24 mg/ml for [RGRGG]₅) and titrated against poly(A) RNA. Samples were prepared using the same buffer as the solution turbidity measurements. Each sample was incubated at room temperature for ~ 2 minutes.

Partition coefficient measurements: Peptide-RNA mixtures were prepared at the desired concentration and composition and subsequently injected into a tween 20-coated (20% v/v) 25 mm x 75 mm x 0.1 mm single chamber custom-made flow-cell. Samples were made at 0.24 mg/ml (100 μ M) [RGRGG]₅ peptide concentration and variable RNA concentration in 25 mM Tris-HCl buffer, 25 mM NaCl, 20 mM DTT (pH 7.5). Confocal imaging was performed using a laser scanning confocal fluorescence microscope (LUMICKSTM C-trap, 60x water-immersion objective). Images were analyzed using the Fiji software⁷. For samples in the single phase region, the partition was taken to be 1.0. For the phase separated sample, partition coefficient (k) was calculated using the following equation:

$$k = \frac{\text{mean intensity per unit area of droplets}}{\text{mean intensity per unit area of the dilute phase}}$$

The partition coefficient estimation was carried out for several droplets per sample for statistical accuracy using Microsoft Excel. Intensity profile plots were generated using OriginPro software.

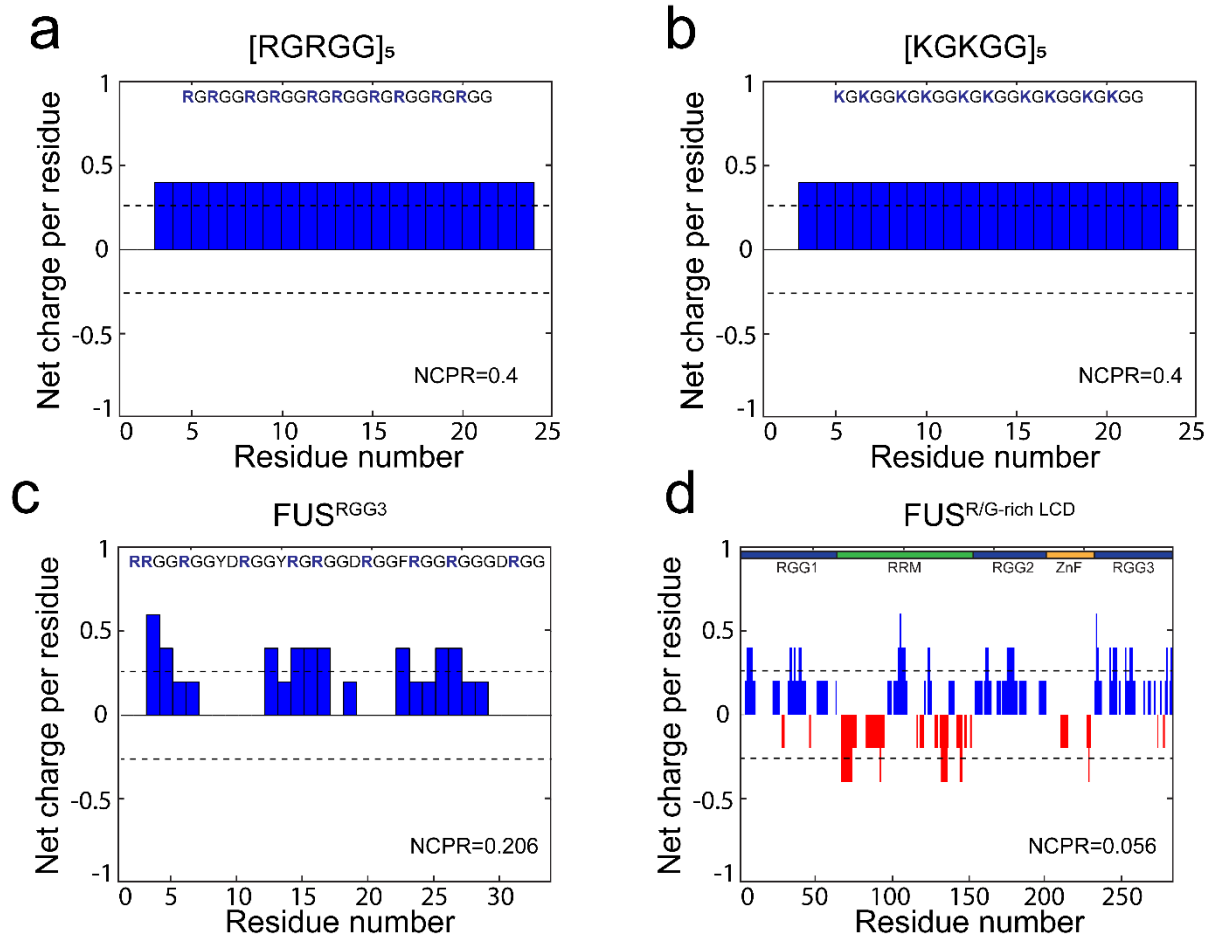


Figure S2 : Net charge per residue (NCPR) distribution for **(a)** $[RGRGG]_5$, **(b)** $[KGKGG]_5$, **(c)** FUS^{RGG3} , and **(d)** $FUS^{R/G-rich LCD}$. NCPR was estimated using the CIDER algorithm⁸.

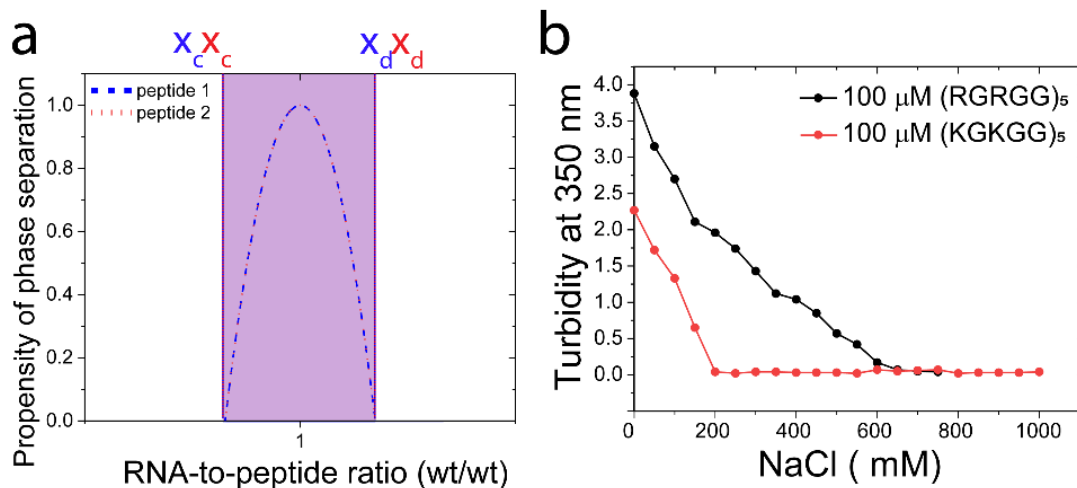


Figure S3: (a) Propensity of phase separation for two peptides of the same charge calculated from *equation-9* in **SI-note 1**. The two curves here represent the values of the RNA-to-peptide ratio at which the inter-complex attraction leading to phase separation is favorable. They correspond to the absolute value of the relative energy loss due to phase separation, which is maximal at RNA-to-peptide ratio of 1.0. In regions outside the boundary marked by x_c and x_d , phase separation is not favorable. See SI Note-1 for further details. Shaded region shows the RNA-to-peptide ratio in which phase separation is favorable. (b) Solution turbidity at 350 nm for independently prepared mixtures of $[\text{RGRGG}]_5$ ($100 \mu\text{M}$ or 0.24 mg/ml ; black) and $[\text{KGKGG}]_5$ ($100 \mu\text{M}$ or 0.22 mg/ml ; red) with poly(U) RNA at 1:1 ratio (wt/wt) as a function of salt concentration. Buffer condition: 25 mM Tris-HCl, 20 mM DTT (pH 7.5) with variable NaCl concentrations as indicated in the plot.

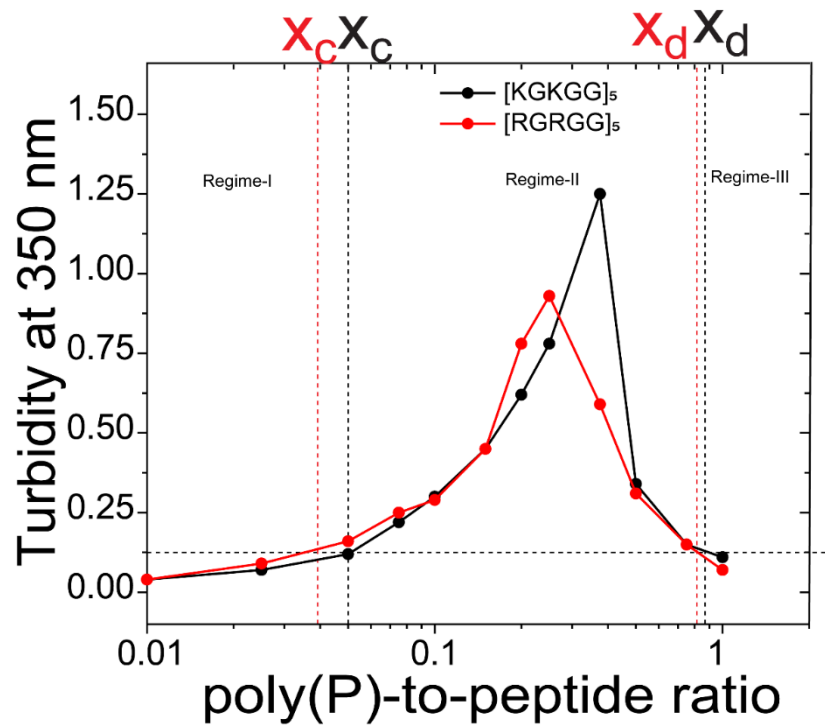


Figure S4: Solution turbidity at 350 nm for [RGRGG]₅ and [KGKGG]₅ as a function of polyphosphate (polyP)-to-peptide ratio (wt/wt). Peptide concentration: 100 μ M, buffer: 25 mM Tris-HCl, 20 mM DTT (pH 7.5). For these measurements, polyP₁₀₀ was used.

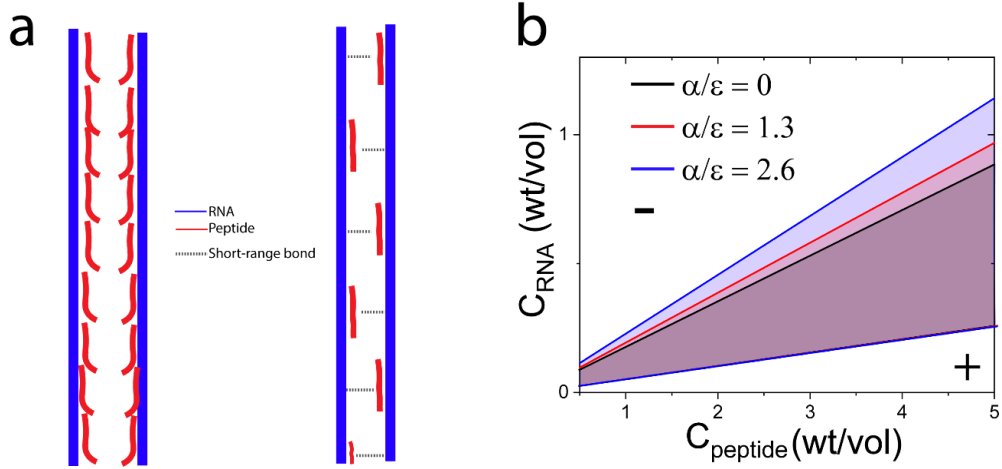


Figure S5: (a) Proposed scheme of over-screened complexes (left) with minimal short-range inter-complex cation- π attraction and under-screened complexes (right) with significant inter-complex cation- π attraction. (b) Theoretical phase diagrams (calculated using the extended RLC model). By taking structural differences into account, the phase diagram with different values of the short-range attraction strength α exhibits an asymmetric shift in decondensation boundary similar to what is observed in experiments (Figure 2 in the main text; SI Note-1). The negative and positive signs indicate the overall charges of the complexes. Parameters used are: $Q = 1000$, $q = 2$, $\epsilon = 600$, $\beta = 0.5$.

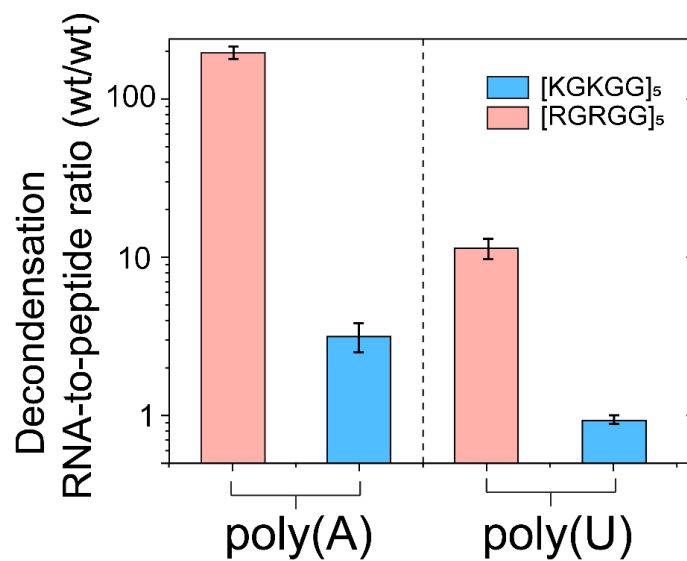


Figure S6: Decondensation boundaries corresponding to the emergence of a reentrant phase (from the macroscopic turbidity assay data presented in Figure 2 in the maintext). The error bars were taken as the range of decondensation values from several turbidity titrations. The values were determined by the solution having an absorbance value (A_{350}) of less than 0.25.

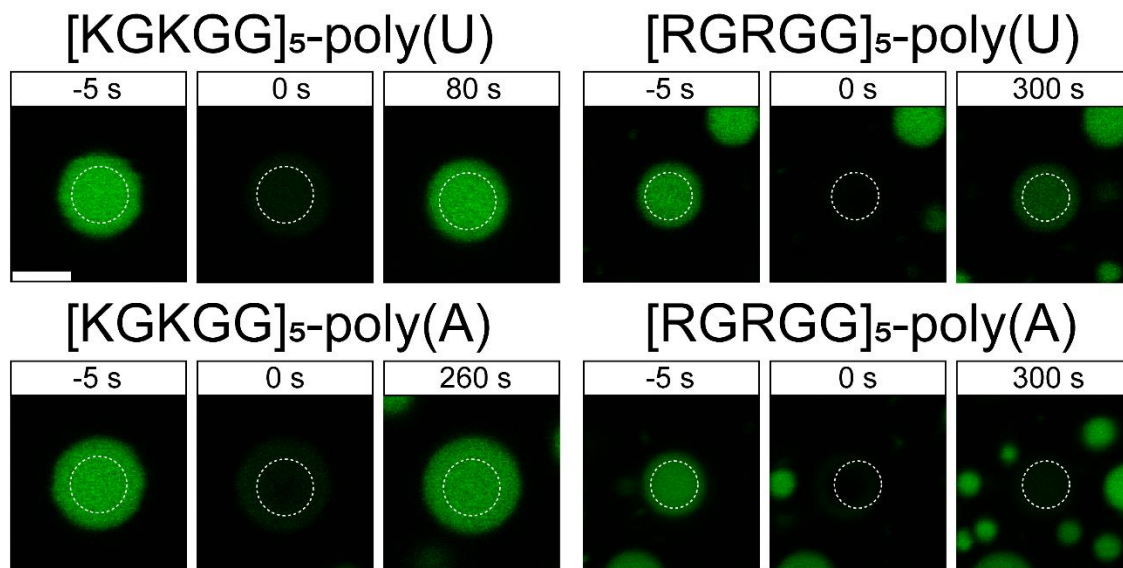


Figure S7: Time-lapse FRAP images for various peptide-RNA condensates. Negative time points indicate pre-bleaching times (bleaching occurs at $t=0$ s). Scale bar represents 5 μm . The FRAP plots are shown in Fig. 4a in the maintext. All samples for FRAP measurements were prepared at 1.0 mg/ml peptide concentration, 0.75 mg/ml RNA concentration (corresponding to the peak in their turbidity plots shown in Fig. 2c-e) and a buffer (25 mM Tris-HCl, 20 mM DTT, 25 mM NaCl (pH 7.5)).

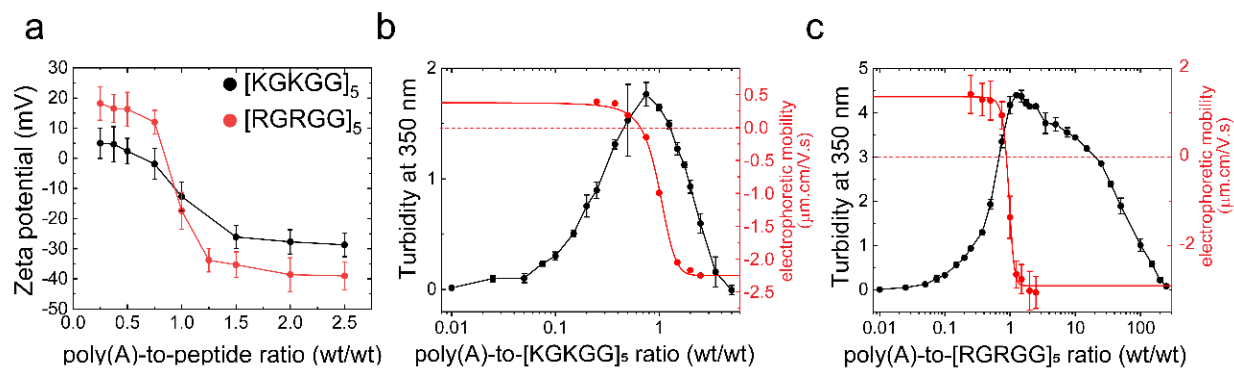


Figure S8: (a) Zeta potential of peptide-RNA mixtures for [RGRGG]₅ (red) and [KGKGG]₅ (black) with poly(A) RNA at variable composition. (b) Overlay plot of turbidity at 350 nm (left axis, black) and electrophoretic mobility (right axis, red) for poly(A)-[KGKGG]₅ mixture. (c) Overlay plot of turbidity at 350 nm (left axis, black) and electrophoretic mobility (right axis, red) for poly(A)-[RGRGG]₅ mixtures. (buffer: 25 mM Tris-HCl, pH 7.5, containing 20 mM DTT).

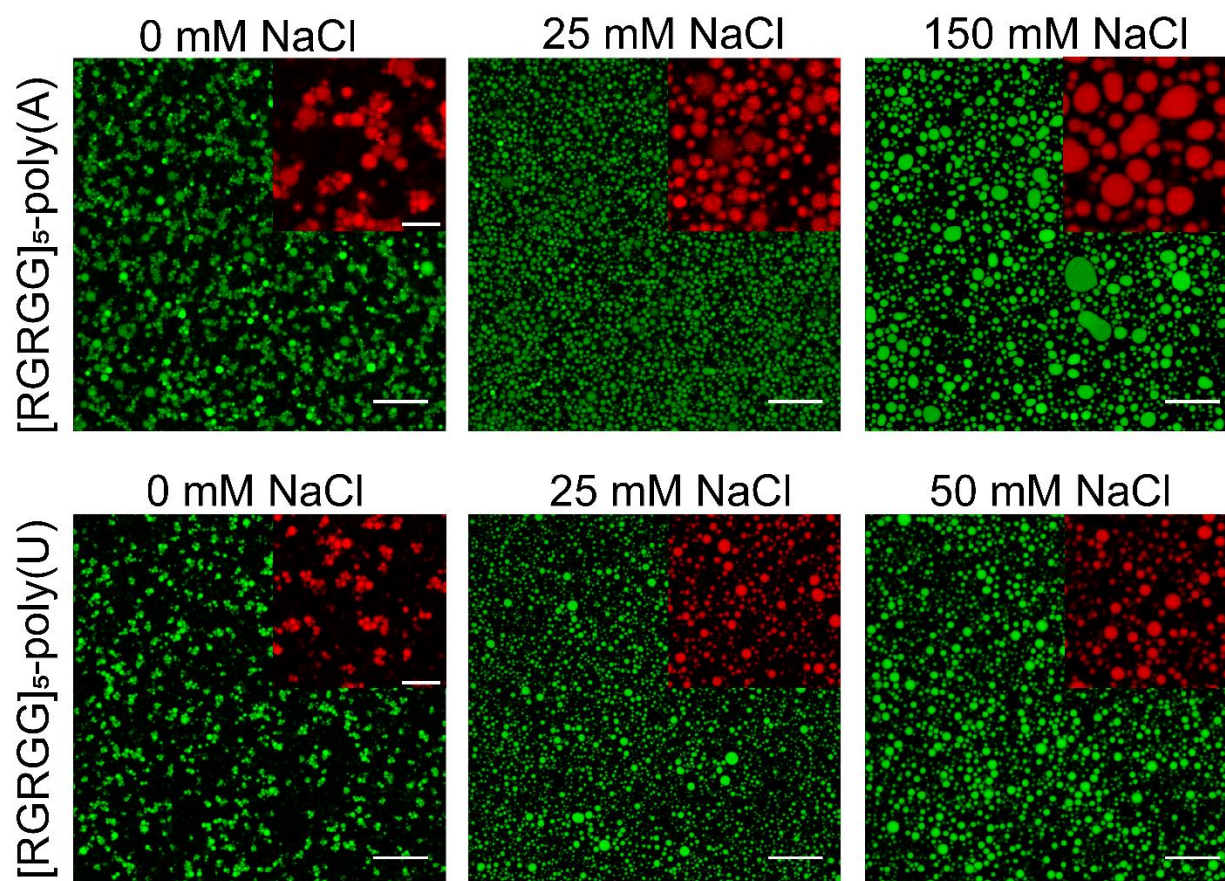


Figure S9: Gel-like droplet clusters transition to a liquid-like phase with increasing salt concentration. Shown here are droplet clusters formed by poly(A)-[RGRGG]₅ mixture (upper panel) and poly(U)-[RGRGG]₅ mixture (lower panel). Poly(A) samples were prepared at 2.0 mg/ml [RGRGG]₅, 10 mg/ml poly(A) in 10 mM Tris-HCl, 20 mM DTT (pH 7.5) buffer and images are shown for 0 mM, 25 mM and 150 mM NaCl concentrations (from left to right). Poly(U) samples were prepared at similar peptide/RNA concentrations in 5.0 mM Tris-HCl buffer (pH 7.5), 20 mM DTT and images are shown for 0 mM, 25 mM and 50 mM salt (left to right). The *insets* are zoomed in view with pseudocolored red for better clarity. Scale bar represents 20 μ m (green images) and 10 μ m (red images), and are shown only for the first image in each panel. The rest of the images in a given sequence follow the same scale bar as the initial image.

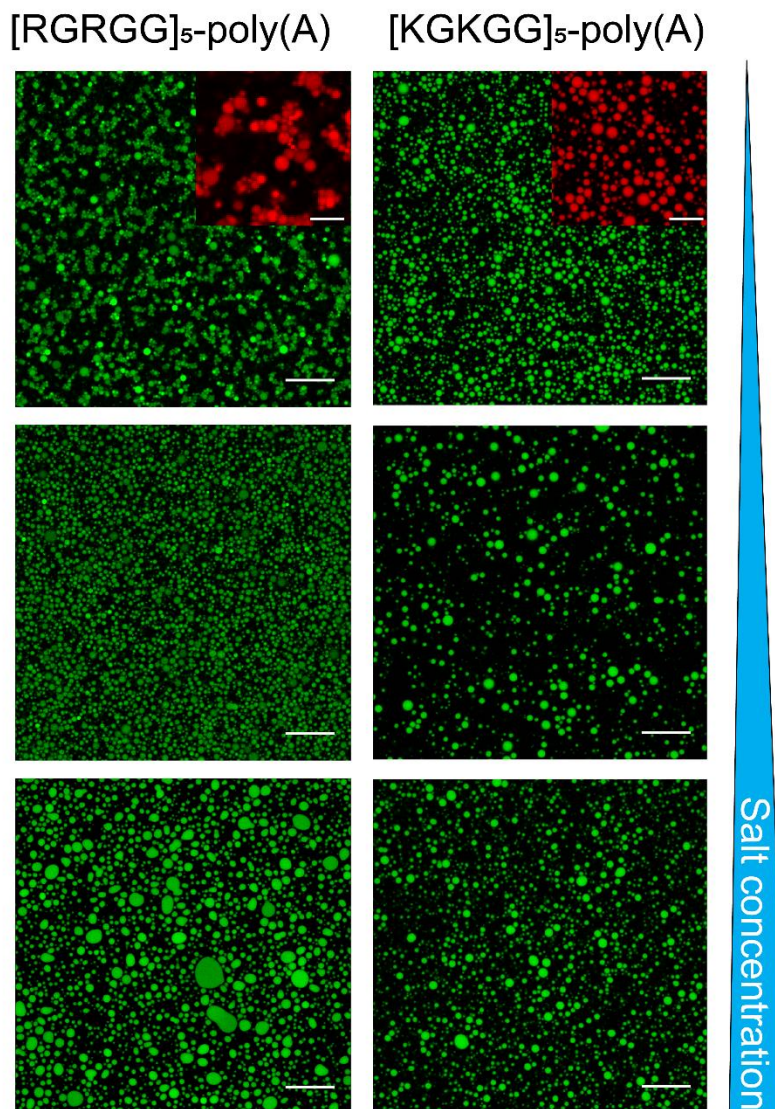


Figure S10: Fluorescence micrographs showing droplet clusters (or a lack thereof) as a function of salt. **Left panel:** Gel-like poly(A)-[RGRGG]₅ droplet clusters transition to a liquid-like droplet suspension with increasing buffer ionic strength. poly(A)-[RGRGG]₅ samples were prepared at 2.0 mg/ml [RGRGG]₅, 8.0 mg/ml poly(A) in 10 mM Tris-HCl, 20 mM DTT (pH 7.5) buffer and images are shown for 0 mM, 25 mM and 150 mM NaCl concentrations (from top to bottom). **Right panel:** poly(A)-[KGKGG]₅ mixtures displaying a liquid-like droplet suspension at low salt buffer (10 mM Tris-HCl, pH 7.5, 20 mM DTT). The droplet density and size are altered with increasing buffer ionic strength. poly(A)-[KGKGG]₅ samples were prepared using 2.0 mg/ml peptide and 8.0 mg/ml poly(A). Salt concentrations used are 0, 25, and 50 mM NaCl (from top to bottom), respectively. Scale bar is 20 μ m for green images and 10 μ m for red images. The *insets* are zoomed-in view (pseudocolored red) for better clarity.

SI Note-1

Our experimental data suggest that short-range attraction only affects the phase boundary where RNA is in excess ($[RNA] \gg [peptide]$), while leaving the other phase boundary ($[RNA] \ll [peptide]$) unchanged (Fig. 2 in the Main Text). Here, we propose a model to qualitatively capture the features of the phase boundary curves obtained experimentally. Our framework utilizes the work of Nguyen and Shklovskii where a charge inversion mechanism for reentrant phase transition was considered⁹. We will discuss a system of long polyanion (RNA) and large positively charged spheres (representing the peptides). We will first present the theory without accounting for short-range attractions. Then we will introduce necessary modifications to include the short-range attraction in the free energy expressions to recapitulate the experimental observations.

Before we start setting up the model, we will discuss the fundamental ideas of the charge inversion mechanism. This phenomenon is a manifestation of ion-ion correlations. Consider the problem of Z -valent ions condensing on an oppositely charged surface. We are interested in understanding the energetic components that are relevant when transferring a Z -ion from the bulk solution to the oppositely charged surface (such surface will be considered as the surface of an RNA chain subsequently). The obvious way to solve this problem is by considering the Poisson-Boltzmann equation and solving it for the concentration profile near the surface. This approach fails when $Z > 1$ and correlation effects have to be considered¹⁰. When Z -ions condense on the surface, due to their high charge, they experience lateral repulsion between each other in addition to the attraction to the oppositely charged surface. The lateral repulsion between Z -ions leads them to reconfigure their position to maximize the average distance between ions in order to reduce the repulsive energy. In situations where the screening length is large, such reconfiguration is of key importance. The resulting configuration behaves as a Wigner crystal or a strongly correlated liquid (SCL)¹¹. The chemical potential of such a liquid has two parts, one comes from a similar two dimensional system of an ideal gas, and one stemming from the energy of a Wigner crystal¹⁰

$$\mu_c = \mu_{id} + \mu_{wc}$$

The contribution of the Wigner crystal term is entirely due to ion-ion correlation. When a Z -ion is moved from the bulk to the solution, the change in chemical potential contains two terms. The first is the change in the potential energy. Z -ions in the bulk often come close to each other due to thermal fluctuations, which renders a positive average repulsive energy per Z -ion. On the other hand, on the surface, lateral repulsions ensure that the Z -ion is always at a maximum distance from other ions (the radius of the Wigner-Seitz cell¹²) which reduces the average repulsive energy per Z -ion. Moreover, there is a loss in kinetic energy since the lateral repulsive forces ensure that the Z -ion remains inside its Wigner-Seitz cell. This loss in kinetic energy is often translated to a loss in entropy. The SCL is stable when the change in the repulsive energy exceeds the change in the kinetic energy of the molecule. This case is often true for Z -ions and also for low temperatures, while it is not true for monovalent ions¹⁰. The energy-gain due to the formation of two dimensional strongly correlated liquid is known as the correlation energy. The conclusion is that the correlation energy is always negative once an SCL is stable. When ions reconfigure themselves non-randomly, the repulsive energy and entropy decrease. Therefore, a correlated configuration would be thermodynamically favored in systems where the repulsive energy is high, temperature is low, and a system consist of large particles (entropy cost is small). This case applies to Z -ions, charged macro-ions and low temperature systems.

To further illustrate this correlation energy physically, it is most clear when the surface is neutralized with a certain concentration of Z-ions. The surface along with its neutralizing layer of Z-ions can be considered as a conducting plane. This is because of the discreteness of the charges of the neutralizing layer allows reconfiguring the positions of the ions similar to the reconfiguration of electrons on a metal. When a Z-ion approaches such a neutralizing surface, it repels the ions on the surface creating a correlation hole (or an image charge). Then the Z-ion is attracted to the correlation hole even though the surface is neutral. Such attraction is responsible for the surface charge inversion. Without strong correlations, the Z-ions would not feel the neutral surface attraction since the configuration of the neutralizing layer would be random and uncorrelated, which is true in the case of monovalent small ions¹².

Another emergent phenomenon from strong correlation is the attraction between two surfaces covered with a neutralizing Wigner crystal (or SCL). This attraction was suggested to drive the condensation or phase separation of large polyelectrolytes such as DNA condensation by multivalent counterions^{9, 13}.

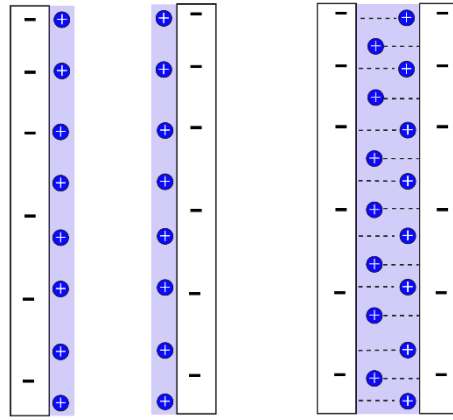


Figure S11: Correlation energy is increased by merging the two layers due to more interactions of ions with the negative background charge of the opposite surface.

To understand this, consider two surfaces at a short distance from each other and neutralized by a layer of SCL having n ions. In the separated state, each ion interacts with the background charge of its corresponding surface, as well as experiencing correlation effects from $n - 1$ ions. When merging the two SCLs into one layer, the energy per Z-ion coming from ion-ion correlations changes since each ion is now interacting with $2n - 1$ ions (Fig. S11). The question is: what is the dependence of the correlation energy on the number of ions n ? The answer is given by the expression for the correlation energy of a Wigner crystal¹²

$$E(n) = -1.96 \frac{n^{\frac{1}{2}} Z^2 e^2}{\epsilon}$$

Therefore, the conclusion is that doubling the number of Z-ions by merging the two layers increases the correlation energy, which in turn leads to attraction between the two surfaces. This attraction is what drives DNA, RNA, and in general polyelectrolyte condensation in this framework. Furthermore, correlation effects have been shown to induce attraction even between like-charged complexes, which is expected to be the reason behind the reentrant condensation observed in many electrostatically driven phase separating systems^{3, 14, 15}. All of the aforementioned arguments hold true not only for plane surfaces, but also for

spherical and cylindrical surfaces as well¹⁶. Therefore, we shall start setting this model by considering the RNA chain to be a strongly charged cylinder interacting with positive large spheres (or peptide globules).

Consider a system composed of negatively charged RNA, positively charged spheres and a solvent. Let p be the chain concentration of RNA, s be the concentration of the positive spheres, $-Q$ be the charge on an RNA chain and q be the charge on a sphere. We define the quantity N as the number of spheres absorbed to a single RNA chain, and $N_i = Q/q$ as the number of spheres required to be absorbed onto an RNA chain such that the total charge on the sphere-RNA complex is zero. A sphere-RNA complex can be thought of as a cylindrical capacitor with net charge Q^* and capacitance C . The free energy of a single sphere-RNA complex is given by

$$f(N) = \frac{Q^{*2}}{2C} + NE(N) \quad (1)$$

Where $E(N)$ is the correlation energy per sphere on the complex. The first term is the repulsive coulomb energy due to the charge on the complex, the second term is the negative correlation energy due to spheres binding to RNA. The effective charge and the capacitance of the complex are given by⁹

$$Q^* = qN - Q = \left(\frac{N}{N_i} - 1\right) Q \quad (2)$$

$$C = \frac{DL}{2 \ln\left(\frac{r_s}{l} + 1\right)} \quad (3)$$

Where D is the dielectric constant of the solvent, L is the length of the chain, r_s is the Debye length and l is the average distance between two neighboring spheres. These expressions are obtained by considering the complex as a charged cylinder. When a complex is neutral, it can attract other neutral complexes via short-range electrostatic correlation energy $N_i \epsilon_{corr}$. This attractive energy drives the condensation of complexes into droplets under certain conditions. Let x be the fraction of complexes aggregating into a condensate, the free energy of the system can be written as

$$F = (1-x)pf(N) + xpN_i(E(N_i) + \epsilon) + k_B T (s - xpN_i - (1-x)Np) \ln \frac{(s - xpN_i - (1-x)Np)}{e} \quad (4)$$

Where $\epsilon = \epsilon_{corr}$. The first term in (4) is the energy of free charged complexes, the second term is the energy of complexes in the condensate and the last term is the entropy of free spheres in the solution. We note that the entropy of the RNA chains is ignored due to their large size. Minimizing this free energy with respect to x yields

$$\epsilon N_i = \frac{Q^2 \left(\frac{N}{N_i} - 1\right)^2}{2C} + NE(N) - N_i E(N_i) + (N_i - N)kT \ln (s - xpN_i - (1-x)Np) \quad (5)$$

To evaluate $NE(N) - N_i E(N_i)$, a Taylor series expansion around $N = N_i$ can be employed

$$NE(N) = N_i E(N_i) + (N - N_i) \frac{\partial(NE(N))}{\partial N} \Big|_{N=N_i}$$

$$NE(N) - N_i E(N_i) = (N - N_i) \mu_c(N_i)$$

Where $\mu_c(N) = \frac{\partial(NE(N))}{\partial N}$. This leads to

$$\epsilon N_i = \frac{Q^2 \left(\frac{N}{N_i} - 1 \right)^2}{2C} + (N_i - N) [kT \ln(s - xpN_i - (1-x)Np) - \mu_c(N_i)] \quad (6)$$

Minimizing the free energy in (4) with respect to N yields

$$kT \ln(s - xpN_i - (1-x)Np) = \frac{Q^2}{CN_i} \left(\frac{N}{N_i} - 1 \right) + \mu_c(N) \quad (7)$$

Equation (6) is the equilibrium condition between free complexes and condensed complexes. Equation (7) represents the equilibrium between free spheres and spheres bound to an RNA chain. Combining the two equations yields:

$$\epsilon N_i = \frac{Q^2 \left(\frac{N}{N_i} - 1 \right)^2}{2C} + (N_i - N) \left[\frac{Q^2}{CN_i} \left(\frac{N}{N_i} - 1 \right) + \mu_c(N) - \mu_c(N_i) \right] \quad (8)$$

Here, we make the assumption that near the condensation conditions, the charge on complexes are almost neutral, hence $\mu_c(N) \cong \mu_c(N_i)^{9, 16, 17}$. Note that ϵ has a negative value. Using these assumptions and the expression in (2), equation (8) can be written as

$$|\epsilon| = \frac{qQ}{C} \left(1 - \frac{N}{N_i} \right)^2 \quad (9)$$

This equation suggests that taking a complex from the free dilute state to a droplet, the system loses an energy $|\epsilon|$ due to complex-complex attraction but increases the total repulsive energy by $\frac{qQ}{C} \left(1 - \frac{N}{N_i} \right)^2$ due to having one less complex to share the total charge of the solution. Depending on the balance between the two contributions, condensation or dissolution is decided. Figure S12a shows the difference between the two energies $f_{cond} = \frac{qQ}{C} \left(1 - \frac{N}{N_i} \right)^2 - |\epsilon|$ as a function of the number of spheres per RNA molecule N . Note that the equality (9) holds at the critical points. Solving for N from (9) we get

$$N_{c,d} = N_i \left(1 \mp \sqrt{\frac{|\epsilon|C}{qQ}} \right) \quad (10)$$

To get the concentration of spheres at which condensation occurs, we look at the limit when the RNA concentration is small. In that limit, equation (7) can be written as

$$kT \ln \frac{s}{s_0} = \frac{Q^2}{CN_i} \left(\frac{N}{N_i} - 1 \right) \quad (11)$$

Where s_0 is defined as

$$s_0 = \exp \left(- \frac{|\mu_c(N_i)|}{kT} \right) \quad (12)$$

Substituting (12) in (9)

$$\frac{|\epsilon|}{kT} = \frac{kTC}{2qQ} \ln^2 \frac{s}{s_0} \quad (13)$$

This equation can be solved for the critical concentration s_c and s_d .

To produce a phase diagram, the dependence of s_c and s_d on p has to be derived. Equation (10) tells us that the number of spheres per complex at the boundaries N_c and N_d is independent of the RNA concentration p . Hence, by inspecting equation (7), which relates the free sphere concentration $s - xpN_i - (1 - x)pN$ to the number of spheres per RNA molecule N , we conclude that the free sphere concentration is independent of p in the condensation/decondensation boundary. In the small p limit, almost all spheres are free. When the sphere concentration is higher than s_c and lower than s_d , condensation is favorable. Therefore, one can postulate that near condensation/decondensation boundary, the concentration of free spheres in the system has to equal the critical concentration for condensation/decondensation boundaries, i.e.

$$s(x, p) - xpN_i - (1 - x)pN_c = s_c \quad (14)$$

$$s(x, p) - xpN_i - (1 - x)pN_d = s_d \quad (15)$$

and by setting $x = 0$ for the two boundaries (i.e., when complex start to aggregate and when aggregates dissolve completely) we get

$$s_c(p) = s_c + pN_c \quad (16)$$

$$s_d(p) = s_d + pN_d \quad (17)$$

This equation is valid for all values of p since we established that N_c/N_d are independent of p .

So far, we established the current model for reentrant phase transition. The input parameters of this model are ϵ and s_0 , which can be determined experimentally. If we add a simple inter-complex short-range attraction ϵ_{sh} , then $\epsilon = \epsilon_{corr} + \epsilon_{sh}$, which results in a symmetric widening of the LLPS region that is shown in Fig. 3c&d in the main text. Our experiments, however, show an asymmetric widening of the condensation regime (Fig. 2 main text). We now wish to incorporate the effects of other short-range forces such as the cation- π attraction explicitly in the free energy equations. This is represented by a short-range attractive energy between the spheres and the RNA chain. Given our discussion in the introduction of this Note, we would expect several effects due to this short-range attraction. First, the propensity of charge inversion would increase since now we have an extra force of attraction between a sphere and its correlation hole. Moreover, we would expect that inter-complex attraction would increase as a result of such attractive force. In addition, the effect of increased short-range force would be prominent only in the case where

complexes are under-screened (excess RNA). This is due to the distinct microscopic nature of under-charged versus over-charged complexes as we shall discuss later. Let us first modify the free energy to include a term for short-range attraction and follow the same procedure outlined above to produce a phase diagram for different strengths of the short-range attraction. The energy of a free charge complex in equation (1) can be modified to

$$f(N) = \frac{Q^{*2}}{2C} + NE(N) + NE_{sh}(N) \quad (18)$$

And the total free energy of the system can be given by

$$F = (1-x)pf(N) + xpN_i(E(N_i) + E_{sh}(N_i) + \epsilon) + k_B T (s - xpN_i - (1-x)Np) \times \ln \frac{(s - xpN_i - (1-x)Np)}{e} \quad (19)$$

Following identical steps for minimizing the free energy with respect to x and N , one gets the modified equilibrium conditions

$$kT \ln(s - xpN_i - (1-x)Np) = \frac{Q^2}{CN_i} \left(\frac{N}{N_i} - 1 \right) + \mu_c(N) + \mu_{sh}(N) \quad (20)$$

$$\epsilon N_i = \frac{Q^2 \left(\frac{N}{N_i} - 1 \right)^2}{2C} + (N_i - N)[kT \ln(s - xpN_i - (1-x)Np) - \mu_c(N_i) - \mu_{sh}(N_i)] \quad (21)$$

Where $\mu_{sh}(N) = \frac{\partial}{\partial N} (NE_{sh}(N))$. Combining the two equations along with using the assumption $\mu_c(N) \cong \mu_c(N_i)$ we get,

$$\epsilon = \frac{Q^2 \left(\frac{N}{N_i} - 1 \right)^2}{2CN_i} + \left(1 - \frac{N}{N_i} \right) \left[\frac{Q^2}{CN_i} \left(\frac{N}{N_i} - 1 \right) + \mu_{sh}(N) - \mu_{sh}(N_i) \right] \quad (22)$$

$$|\epsilon| = + \frac{qQ}{2C} \left(\frac{N}{N_i} - 1 \right)^2 - \left(1 - \frac{N}{N_i} \right) [\mu_{sh}(N) - \mu_{sh}(N_i)] \quad (23)$$

Equation (23) is the modified form of equation (9) upon introducing the short-range force. The second term on the right hand side of equation (23) is the gain in short-range energy as complexes go from the free state to the droplet state. The interpretation is similar, when transferring a complex from the free state to the droplet state, the free energy is lowered by the correlation energy $|\epsilon|$ while it gets a positive correction from the repulsive coulomb energy. The magnitude of the correction due to short-range attractions depends on whether complexes are under screened ($\frac{N}{N_i} < 1$) or overscreened ($\frac{N}{N_i} > 1$). This asymmetry is the fundamental difference between the short-range correction and the electrostatic coulomb correction, since the latter is always positive regardless of the screening state of the complex.

The exact form of $E_{sh}(N)$ is beyond the scope of the present work, and may be calculated from a microscopic theory. However, certain features of this function can be argued for. Let us consider the electrostatic repulsive energy of a complex as a function of the number of spheres per RNA chain N . When

$N \ll N_i$ the total charge is negative and the repulsive energy is high. Upon increasing N , the charge on the complex approaches to zero as well as the repulsive energy. Beyond the neutral point $N = N_i$, the charge on the complex becomes positive and the repulsive energy grows with further increasing N .

For the short-range interaction, the energy increases with N when the complex is not completely screened ($N \ll N_i$) due to the exposed RNA bases. Upon approaching the neutral point, the short-range interaction approaches a saturation point since all RNA bases are already engaged in short-range bonding with the peptides. Beyond the neutral point ($N = N_i$), increasing N does not increase the short-range interaction energy significantly since all of the RNA bases are already engaged in the short-range attraction with the peptide (Fig. S5a). In other words, there is a finite number of short-range bonds an RNA chain can have with the peptide, and that number is fully satisfied at $N = N_i$. Increasing the number of peptides further would only cause the repulsive energy to grow but not the short-range energy. It is therefore reasonable to expect that the short-range interaction energy $NE_{sh}(N)$ should increase rapidly at low $\frac{N}{N_i}$ and should approach a plateau near $\frac{N}{N_i}=1$. We propose a candidate function that satisfies these conditions

$$NE_{sh}(N) = \frac{\eta}{\beta N_i} \frac{N}{1 + \frac{N}{\beta N_i}} \quad (24)$$

Where η is a parameter representing the strength of the short-range attraction and β represents the saturation parameter (Fig. S12b). The mathematical form of equation (24) is inspired by a two dimensional adsorption model. If we consider the peptides to form a liquid on the surface of RNA, then one can argue that the surface coverage, or the probability of an RNA base being engaged in a cation- π interaction, can be described by a Langmuir isotherm¹⁸. Therefore, we estimate the short-range energy of a complex by multiplying the strength parameter η by the surface coverage or the probability of binding. Consequently, the chemical potential is

$$\mu_{sh}(N) = \frac{\partial(NE_{sh}(N))}{\partial N} = \frac{\eta}{\beta N_i} \frac{1}{\left(1 + \frac{N}{\beta N_i}\right)^2} = \alpha \frac{1}{\left(1 + \frac{N}{\beta N_i}\right)^2} \quad (25)$$

Where $\alpha = \frac{\eta}{\beta N_i}$. Hence by substituting in equation (23) we get

$$|\epsilon| = \frac{qQ}{C} \left(1 - \frac{N}{N_i}\right)^2 - \left(1 - \frac{N}{N_i}\right) \alpha \left(\left(1 + \frac{N}{\beta N_i}\right)^{-2} - \left(1 + \frac{1}{\beta}\right)^{-2} \right) \quad (26)$$

let f_{cond} be the difference between the two hand sides of equation 26

$$f_{cond} = \frac{qQ}{C} \left(1 - \frac{N}{N_i}\right)^2 - \left(1 - \frac{N}{N_i}\right) \alpha \left(\left(1 + \frac{N}{\beta N_i}\right)^{-2} - \left(1 + \frac{1}{\beta}\right)^{-2} \right) - |\epsilon| = 0$$

When $f_{cond} = 0$, equation (26) is satisfied and we get the boundaries of condensation/decondensation (N_c and N_d). Plotting f_{cond} as a function of N for several values of the strength of the short-range interaction α , we see that the condensation boundary is shifted by a large margin compared with the decondensation

boundary (Fig. S12c). More generally, the phase boundary near the under-screened (negative) complexes is more sensitive to the short-range attraction than the phase boundary near the over-screened side. Such difference is due to the saturation of short-range attraction energy beyond the neutral point. We solved equation (26) numerically for several values of the short-range attraction, and used equation (14) and (15) to generate a phase diagram shown in Figure S5b for the sphere-RNA system in presence of short-range attraction. We note that the evaluation of the intercepts s_c and s_d is ignored since it is only relevant at very small RNA concentrations and would slightly shift the lines upwards. In other words, we have assumed that all spheres are bound to an RNA chain for the purposes of plotting the phase diagram¹⁷. The important variable is the slope of the line, which corresponds to N_c and N_d as determined by equation (26).

In the phase diagrams obtained by experiments (Fig. 2 in main-text), the phase boundary where the complexes are negatively charged is more sensitively dependent on the short-range attraction. Our present model has the same feature. Off note, the exact form of $E_{sh}(N)$ is currently unknown, and we simply used a function that satisfies our experimental outcomes. In a sense, the repulsive energy is symmetrical around the neutral point, a hall mark of electrostatics. However, the short-range energy does not have to be symmetrical, it may be saturated when complexes are over-charged due to the finite number of RNA bases that can form short-range cation- π bonds. When an under-screened RNA chain is neutralized, the addition of positive sphere to the chain will result in releasing of repulsive energy and gaining a short-range term between the sphere and the negative RNA segment. However, when an over-screened complex is neutralized, the removal of excess spheres will only release a repulsive energy, and hence, there is only minimal short-range energy gain since more than enough spheres are already present to interact with all the RNA bases. We also speculate that RNA-RNA interactions are also not symmetrical and may contribute to this shift in the boundary.

In conclusion, we used the charge inversion framework to argue that the selective tuning of the phase boundaries can be a result of an asymmetry in the short-range attractive energy as a function of peptide-to-RNA ratio. Our model is consistent with the results of our experiments. The basis of this interpretation is the assumption that the energy gain from short-range attractions approaches saturation beyond the charge neutral point when the complexes are overcharged (Fig. S12b). This is likely due to the absence of exposed RNA monomers to the condensing spheres since all the RNA monomers in the complex are covered with spheres and are already engaged in short-range attractions.

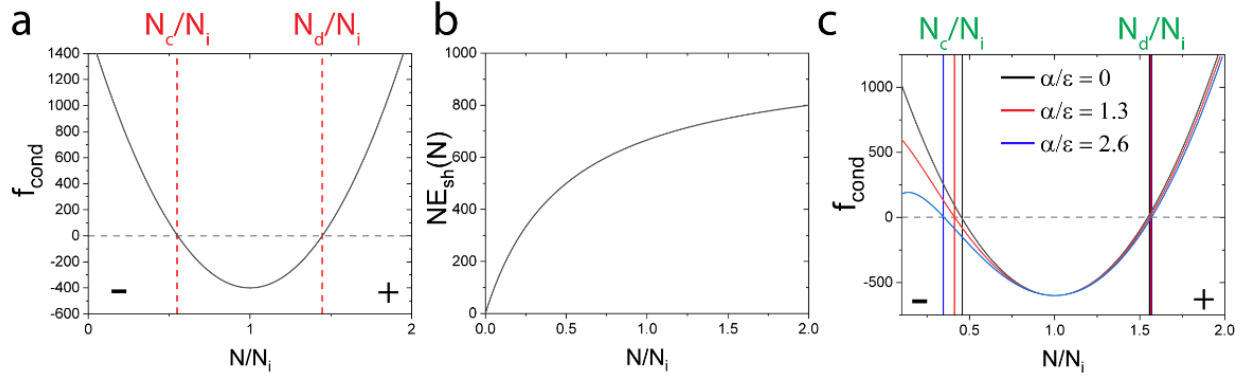


Figure S12: (a) f_{cond} as a function of N/N_i for the case of pure electrostatic forces from equation (9). Condensation occurs when f_{cond} is negative (b) the short-range energy gain for a single sphere-RNA complex as a function of N/N_i ; note that the negative sign is included in equation (26) since it is an attractive force. (c) f_{cond} as a function of N/N_i as with short-range attraction using equation (26). Parameters used are: $Q = 1000, q = 2, \epsilon = 600, \beta = 0.5$.

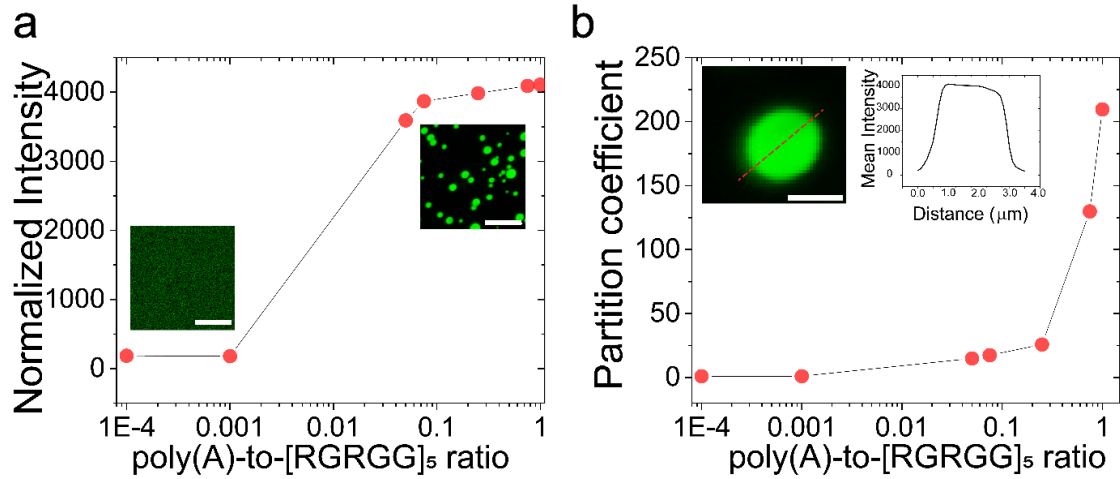


Figure S13: Intensity (a) and partition coefficient (b) analysis during the transition from a mixed phase (regime I) to the condensed phase (regime II) for [RGRGG]₅-poly(A) mixture at a peptide concentration of 0.24 mg/ml. (buffer: 25 mM Tris-HCl, pH 7.5, 20 mM DTT, 25 mM NaCl).

Supplementary Table-1

pH	Sequence net charge			
	[RGRGG] ₅	[KGKGG] ₅	FUS ^{R/G-rich LCD}	FUS ^{RGG3}
6.5	10	10	17.7	7
7	9.9	9.9	16.7	6.9
7.5	9.8	9.7	16	6.8
8	9.5	9.4	15.4	6.5
8.5	9.2	8.9	14.7	6.2

Table S1: Estimated net charge for [RGRGG]₅, [KGKGG]₅, FUS^{R/G-rich LCD}, and FUS^{RGG3}. The corresponding sequences are shown in Supplementary Figure S2. The net charge is estimated using protein calculator v3.4 developed by *C.D Putnam at the Scripps research institute* (<http://protcalc.sourceforge.net/>).

Supplementary Movie Legends:

Supplementary Movies 1-4: Trap-mediated coalescence of suspended droplets of **(1)** [RGRGG]₅-poly(A), **(2)** [RGRGG]₅-poly(U), **(3)** [KGKGG]₅-poly(U), and **(4)** [KGKGG]₅-poly(A). Scale bar represents 1 μm for **(1)** and 2 μm for **(2-4)**.

Supplementary Movies 5-6: Trap-mediated coalescence of suspended droplets of **(5)** FUS^{R/G-rich LCD}-poly(A) **(6)** FUS^{R/G-rich LCD}-poly(U). Scale bar represents 2 μm .

Supplementary Movie 7: Temporal dynamics of [RGRGG]₅-poly(A) droplet clusters. Scale bar represents 10 μm .

Supplementary Movies 8-9: FRAP movies of clusters formed by **(8)** [RGRGG]₅-poly(A) and **(9)** [RGRGG]₅-poly(U). Scale bar represents 10 μm .

Supplementary References

1. Kaur, T.; Alshareedah, I.; Wang, W.; Ngo, J.; Moosa, M. M.; Banerjee, P. R., Molecular Crowding Tunes Material States of Ribonucleoprotein Condensates. *Biomolecules* **2019**, *9* (2), 71.
2. Banerjee, P. R.; Deniz, A. A., Shedding light on protein folding landscapes by single-molecule fluorescence. *Chem Soc Rev* **2014**, *43* (4), 1172-88.
3. Banerjee, P. R.; Milin, A. N.; Moosa, M. M.; Onuchic, P. L.; Deniz, A. A., Reentrant Phase Transition Drives Dynamic Substructure Formation in Ribonucleoprotein Droplets. *Angew Chem Int Ed Engl* **2017**, *56* (38), 11354-11359.
4. Banerjee, P. R.; Mitrea, D. M.; Kriwacki, R. W.; Deniz, A. A., Asymmetric Modulation of Protein Order-Disorder Transitions by Phosphorylation and Partner Binding. *Angew Chem Int Ed Engl* **2016**, *55* (5), 1675-9.
5. Banerjee, P. R.; Moosa, M. M.; Deniz, A. A., Two-Dimensional Crowding Uncovers a Hidden Conformation of alpha-Synuclein. *Angew Chem Int Ed Engl* **2016**, *55* (41), 12789-92.
6. Patel, A.; Lee, Hyun O.; Jawerth, L.; Maharana, S.; Jahnel, M.; Hein, Marco Y.; Stoyanov, S.; Mahamid, J.; Saha, S.; Franzmann, Titus M.; Pozniakovski, A.; Poser, I.; Maghelli, N.; Royer, Loic A.; Weigert, M.; Myers, Eugene W.; Grill, S.; Drechsel, D.; Hyman, Anthony A.; Alberti, S., A Liquid-to-Solid Phase Transition of the ALS Protein FUS Accelerated by Disease Mutation. *Cell* **2015**, *162* (5), 1066-1077.
7. Schindelin, J.; Arganda-Carreras, I.; Frise, E.; Kaynig, V.; Longair, M.; Pietzsch, T.; Preibisch, S.; Rueden, C.; Saalfeld, S.; Schmid, B.; Tinevez, J. Y.; White, D. J.; Hartenstein, V.; Eliceiri, K.; Tomancak, P.; Cardona, A., Fiji: an open-source platform for biological-image analysis. *Nat Methods* **2012**, *9* (7), 676-82.
8. Holehouse, A. S.; Ahad, J.; Das, R. K.; Pappu, R. V., CIDER: Classification of intrinsically disordered ensemble regions. *Biophys J* **2015**, *108* (2), 228a.
9. Nguyen, T. T.; Shklovskii, B. I., Complexation of DNA with positive spheres: phase diagram of charge inversion and reentrant condensation. *J Chem Phys* **2001**, *115* (15), 7298-7308.
10. Perel, V.; Shklovskii, B., Screening of a macroion by multivalent ions: a new boundary condition for the Poisson-Boltzmann equation and charge inversion. *Physica A: Statistical Mechanics and its Applications* **1999**, *274* (3-4), 446-453.
11. Rouzina, I.; Bloomfield, V. A., Macroion attraction due to electrostatic correlation between screening counterions. 1. Mobile surface-adsorbed ions and diffuse ion cloud. *J Phys Chem* **1996**, *100* (23), 9977-9989.
12. Grosberg, A. Y.; Nguyen, T.; Shklovskii, B., Colloquium: the physics of charge inversion in chemical and biological systems. *Rev Mod Phys* **2002**, *74* (2), 329.
13. Nguyen, T. T.; Rouzina, I.; Shklovskii, B. I., Reentrant condensation of DNA induced by multivalent counterions. *J Chem Phys* **2000**, *112* (5), 2562-2568.
14. Nguyen, T. T.; Rouzina, I.; Shklovskii, B. I., Reentrant condensation of DNA induced by multivalent counterions. *J Chem Phys* **2000**, *112* (5), 2562-2568.
15. Zhang, F.; Skoda, M. W.; Jacobs, R. M.; Zorn, S.; Martin, R. A.; Martin, C. M.; Clark, G. F.; Weggler, S.; Hildebrandt, A.; Kohlbacher, O.; Schreiber, F., Reentrant condensation of proteins in solution induced by multivalent counterions. *Phys Rev Lett* **2008**, *101* (14), 148101.
16. Zhang, R.; Shklovskii, B., Phase diagram of aggregation of oppositely charged colloids in salty water. *Phys Rev E* **2004**, *69* (2), 021909.
17. Zhang, R.; Shklovskii, B., Phase diagram of solution of oppositely charged polyelectrolytes. *Physica A: Statistical Mechanics and its Applications* **2005**, *352* (1), 216-238.
18. Butt, H.-J.; Graf, K.; Kappl, M., *Physics and chemistry of interfaces*. Wiley-VCH Verlag: Weinheim, 2013.